
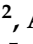







## Article

# Nanoscale Study of the Polar and Electronic Properties of a Molecular Erbium(III) Complex Observed via Scanning Probe Microscopy

Maxim Ivanov <sup>1,\*</sup>, Arkadiusz Grempla <sup>2</sup>, Arseniy Buryakov <sup>3</sup>, Timur Nikitin <sup>4</sup>, Licinia L. G. Justino <sup>4</sup>, Rui Fausto <sup>4,5</sup>, Paula M. Vilarinho <sup>1</sup> and José A. Paixão <sup>6</sup>

<sup>1</sup> Department of Materials and Ceramic Engineering, CICECO—Aveiro Institute of Materials, University of Aveiro, 3810-193 Aveiro, Portugal; paula.vilarinho@ua.pt

<sup>2</sup> Biological and Chemical Research Centre, Faculty of Chemistry, University of Warsaw, 02-089 Warsaw, Poland; a.grempla@uw.edu.pl

<sup>3</sup> Department of Nanoelectronics, MIREA—Russian Technological University, 78 Vernadsky Avenue, 119454 Moscow, Russia; bello16@mail.ru

<sup>4</sup> CQC-IMS, Department of Chemistry, University of Coimbra, Rua Larga s/n, 3004-535 Coimbra, Portugal; tn@u-c.smail.me (T.N.); liciniaj@ci.uc.pt (L.L.G.J.); rfausto@ci.uc.pt (R.F.)

<sup>5</sup> Department of Physics, Faculty Sciences and Letters, Istanbul Kultur University, Bakirkoy, 34158 Istanbul, Turkey

<sup>6</sup> CFisUC, Department of Physics, University of Coimbra, Rua Larga s/n, 3004-516 Coimbra, Portugal; jap@fis.uc.pt

\* Correspondence: ivanovmaxim@ua.pt

**Abstract:** We successfully synthesized millimeter-sized single crystals of the molecular erbium(III) complex  $\text{Er}(\text{acac})_3(\text{cphen})$ , where  $\text{acac}$  = acetylacetonate and  $\text{cphen}$  = 5-chloro-1,10-phenanthroline. The novelty of this work stems from the exhaustive examination of the polar and electronic properties of the obtained samples at the macro-, micro-, and nanoscale levels. The single crystal X-ray diffraction method demonstrates the monoclinic (noncentrosymmetric space group  $P2_1$ ) crystallographic structure of the synthesized samples and scanning electron microscopy exhibits the terrace–ledge morphology of the surface in erbium(III) crystals. By using the piezoelectric force microscopy mode, the origin of the polar properties and the hyperpolarizability in the synthesized samples were assigned to the internal domain structure framed by the characteristic terrace–ledge topography. The direct piezoelectric coefficient ( $\sim d33$ ) was found to be intensely dependent on the local area and was measured in the range of 4–8 pm/V. A nanoscale study using the kelvin probe force and capacitance force (dC/dz) microscopy modes exposed the effect of the Er ions clustering in the erbium(III) complex. The PFM method applied solely to the Er ion revealed the corresponding direct piezoelectric coefficient ( $\sim d33$ ) of about 4 pm/V. Given the maximum piezoelectric coefficient in the erbium(III) complex at 8 pm/V, we highlight the significant importance of the spatial coordination between the lanthanide ion and the ligands. The polar coordination between the lanthanide ion and the nitrogen and oxygen atoms was also corroborated by Raman spectroscopy supported by the density functional theory calculations. The obtained results can be of paramount importance for the application of molecular erbium(III) complex crystals in low-magnitude magnetic or electric field devices, which would reduce the energy consumption and speed up the processing switching in nonvolatile memory devices.

**Keywords:** erbium(III); integrated magnetoelectric molecular system; piezoresponse force microscopy (PFM); kelvin probe force microscopy (KPFM)



**Citation:** Ivanov, M.; Grempla, A.; Buryakov, A.; Nikitin, T.; Justino, L.L.G.; Fausto, R.; Vilarinho, P.M.; Paixão, J.A. Nanoscale Study of the Polar and Electronic Properties of a Molecular Erbium(III) Complex Observed via Scanning Probe Microscopy. *Crystals* **2023**, *13*, 1331. <https://doi.org/10.3390/cryst13091331>

Academic Editor: Juan Ángel Sans

Received: 5 July 2023

Revised: 25 August 2023

Accepted: 28 August 2023

Published: 31 August 2023



**Copyright:** © 2023 by the authors. Licensee MDPI, Basel, Switzerland. This article is an open access article distributed under the terms and conditions of the Creative Commons Attribution (CC BY) license (<https://creativecommons.org/licenses/by/4.0/>).

## 1. Introduction

The development of modern devices suggests using a class of new materials possessing enhanced optical, electrical, and magnetic properties. The decrease in the size of these materials significantly changes their properties towards new and/or coupled

functionality. This ability established a particular way to distinguish the advanced functionality and promote the emersion of hybrid materials, organic/inorganic matrices, and metal–organic frameworks [1,2]. Among others, the exploitation of rare-earth metals (lanthanides) has attracted substantial interest due to their extraordinary optical, electrical, magnetic, electro-, and magneto-optical properties [2]. The photophysical characteristics of lanthanide ions, such as their long-lived emission with a narrow linewidth and broad Stokes shifts (>100 nm) in the visible and near-infrared regions, are the most robust properties attributed to the lanthanide-based complexes [3]. Erbium(III) oxide emits a photon in the visible (545 nm) [4] and infrared ranges (1.54  $\mu\text{m}$  and 2.94  $\mu\text{m}$ ) [5], thus making it useful for OLED and solar energy conversion applications, as well as for biological imaging and detection applications [2]. The 1,10-phenanthroline is usually used in combination with lanthanide to enhance the emitted light, since the strength of the emission is strongly dependent on the ligand surrounding a lanthanide ion owing to the conjugated  $\pi$ -bonds [1,6,7]. Another functionality is the magnetic properties of Er(III)-based complex that can be controlled by external conditions such as light, pressure, and temperature [8,9]. Among these conditions, photochemical control was demonstrated to be the best approach for the Er(III)-based complex with the photoactive ligand bpe, [Er(nat)<sub>3</sub>·MeOH·bpe] (1, bpe = 1,2-bis(2-pyridyl)ethylene, nat = 4,4-trifluoro-1-(2-naphthyl)-1,3-butanedione) due to the accessibility and rapid conduction of light [8]. It was demonstrated that the slight change in the structure around Er(III) ions leads to different magnetic properties, which illustrates the photochemical control of the magnetic properties of single-molecule magnets [8]. The highly sensitive magnetic response of the Er(III)-based complex opens the possibility of linear and nonlinear magneto-optical effects with a distinct application for magneto-optical memory [9]. On the other hand, in complexes, the ligands chelating the lanthanide ion may lead to the organization of the noncentrosymmetric crystallographic packing to assure the polar properties (piezo- or ferroelectrics) [10,11]. The inadequate comprehension of the origins and influence of hyperpolarizability in the linear and nonlinear emission efficiencies of lanthanide complexes, particularly within the near-infrared region, has resulted in a paucity of tangible practical applications [1,3,5,12]. It is important to emphasize that the combination of ferromagnetic and ferroelectric properties results in a magnetoelectric phenomenon. In this phenomenon, the electrical and magnetic systems interact reciprocally such that magnetic properties are controlled by the electric field, and conversely, the electrical properties are regulated by the magnetic field [13–15]. This type of coupling has rarely been declared in multiferroic systems at room temperature, especially in lanthanide-based complexes [15–19]. Being able to modify the polarization or magnetization using either a low-magnitude magnetic or electric field may reduce the needed energy and speed up the processing speed in nonvolatile memory devices [20]. We recently demonstrated an example of a lanthanide-based complex, where the interaction between the rare-earth metal Yb and Zn (R, R-1) resulted in room-temperature magnetoelectric coupling [21]. All the mentioned discoveries open promising prospects for the opportunity to apply rare-earth complexes in opto-, micro-, and nanoelectronics through robustly demonstrated interconnections among optical, electrical, and magnetic properties.

In this work, we successfully synthesized millimeter-sized single crystals of the molecular erbium(III) complex Er(acac)<sub>3</sub>(cphen), where acac = acetylacetonate and cphen = 5-chloro-1,10-phenanthroline. The novelty of this research lies in its comprehensive examination of the polar and electronic properties of the synthesized samples across macroscopic, microscopic, and nanoscopic scales. To achieve this, we employed a diverse array of techniques such as conventional methods like X-ray diffraction and scanning electron microscopy as well as more specialized approaches such as atomic force microscopy, which was further supplemented by Raman measurements. The atomic force microscopy method was implemented in several modes: semicontact force mode for the topography measurements, piezoelectric force mode for the measurements of intrinsic and induced piezo- and ferroelectric properties, kelvin probe mode to study the surface potential distribution, and dC/dz mode for the capacitance distribution. The Raman data were supported by

computation using the density functional theory (DFT) level of theory with the BP86 [22,23] exchange-correlation functional. As a result, we demonstrated the monoclinic (noncentrosymmetric space group  $P2_1$ ) crystallographic structure and terrace–ledge morphology of the obtained molecular erbium(III) complex crystals. By using the piezoelectric force microscopy (PFM) mode, the origins of the polar properties and the hyperpolarizability in the synthesized samples were assigned to the internal domain structure framed by the characteristic terrace–ledge topography. The direct piezoelectric coefficient ( $\sim d_{33}$ ) was found to be intensely dependent on the local area and was measured in the range of 4–8 pm/V. A nanoscale study using kelvin probe force and capacitance force (dC/dz) microscopy modes revealed the effect of clustering in the erbium(III) complex. The PFM method applied solely to the Er ion revealed the corresponding direct piezoelectric coefficient ( $\sim d_{33}$ ) of about 4 pm/V. Considering the maximum piezoelectric coefficient measured in the erbium(III) complex at 8 pm/V, a conclusion on the significant importance of the spatial coordination between the lanthanide ion and the ligands can be made. The coordination between the lanthanide ion and the nitrogen and oxygen atoms was also confirmed by Raman spectroscopy and DFT calculations. We concluded that the role of the spatial coordination between the lanthanide ion and the ligands on the hyperpolarizability and optical properties of lanthanide-based compounds is critical. These results were found to be of very great importance for the application of molecular erbium(III) complex crystals in low-magnitude magnetic or electric field devices to reduce the needed energy and speed up the processing switching in nonvolatile memory devices.

## 2. Experiments

All reagents and solvents were commercially available and used as received without any further purification. In a flask, 0.25 mmol of erbium(III) acetylacetonate hydrate (2,4-Pentanedione erbium(III) derivative,  $\text{Er}(\text{acac})_3$ , 97%, Sigma-Aldrich, St. Louis, MO, USA) was added to 0.25 mmol of 5-chloro-1,10-phenanthroline. The solution was then dissolved in 10 mL of methanol, heated up to 80 °C, and magnetically stirred for five hours. After the reaction was quenched, the final solution was filtered using a syringe filter and recrystallized via a slow evaporation approach at room temperature to obtain good-quality single crystals.

Structural analysis was performed on a millimeter-sized single-crystal, at room temperature, using an APEXII diffractometer (Bruker AXS, Karlsruhe, Germany) equipped with a 4K CCD detector and graphite monochromated  $\text{Mo K}\alpha$  radiation. X-ray characterization of polycrystalline samples was conducted on a Bruker D8 Advance diffractometer, with Ni-filtered  $\text{Cu K}\alpha$  radiation (Bruker, Karlsruhe, Germany). The X-ray diffraction (XRD) patterns were collected in Bragg–Brentano geometry, at room temperature, by scanning in the angle range  $5^\circ \leq 2\theta \leq 30^\circ$  with a step of  $0.02^\circ$  and a dwell of 0.5 s per step. Morphological studies were performed using a high-resolution analytical scanning electron microscope (SEM) VEGA3 (TESCAN Brno, Brno, Czech Republic). The nanoscale properties were measured by scanning probe microscope (SPM) (Ntegra Prima, NT-MDT, Moscow, Russia) implemented in contact (AFM), piezoresponse (PFM), electrostatic (EFM), and kelvin probe (KPFM) force modes. The AFM and PFM methods were used for local topography and piezoelectric properties measurements. The PFM measurements were conducted with an ac voltage frequency of 50 kHz and an amplitude of 10 V. The calibration of the PFM was conducted on the Si substrate following the procedure described in ref. [24]. In order to measure the local switching behavior, the switching spectroscopy PFM (SS-PFM) method was applied. This is a method when after the PFM scan at a predefined local area ( $\sim 2\text{--}30$  nm), dc bias voltage pulses are applied from the minimum to maximum value to detect the switching of the local domain structure. The dc bias voltage applied to the sample during the SS-PFM measurements was varied in the range of 1–50 V. The KPFM at the first and second harmonics were used for the surface charge, surface potential, dielectric permittivity, and dC/dz distribution measurements. Soft cantilevers with force constant at 3 N/m (ElectriMulti75-G, BudgetSensors, Sofia, Bulgaria) coated with Cr/Pt convenient for

electric modes measurements were utilized. The KPFM technique was used to measure the work function (WF) difference between the tip and the sample according to the equation

$$V_{CPD} = \frac{W_{tip} - W_{sample}}{-e} \quad (1)$$

where  $W_{tip}$  is the WF of the SPM tip coating,  $W_{sample}$  is the WF of the sample,  $e$  is the elementary charge, and  $V_{CPD}$  is the measured contact potential difference, viz. surface potential. All the SPM measurements were performed under controlled conditions (25 °C, humidity ~30%).

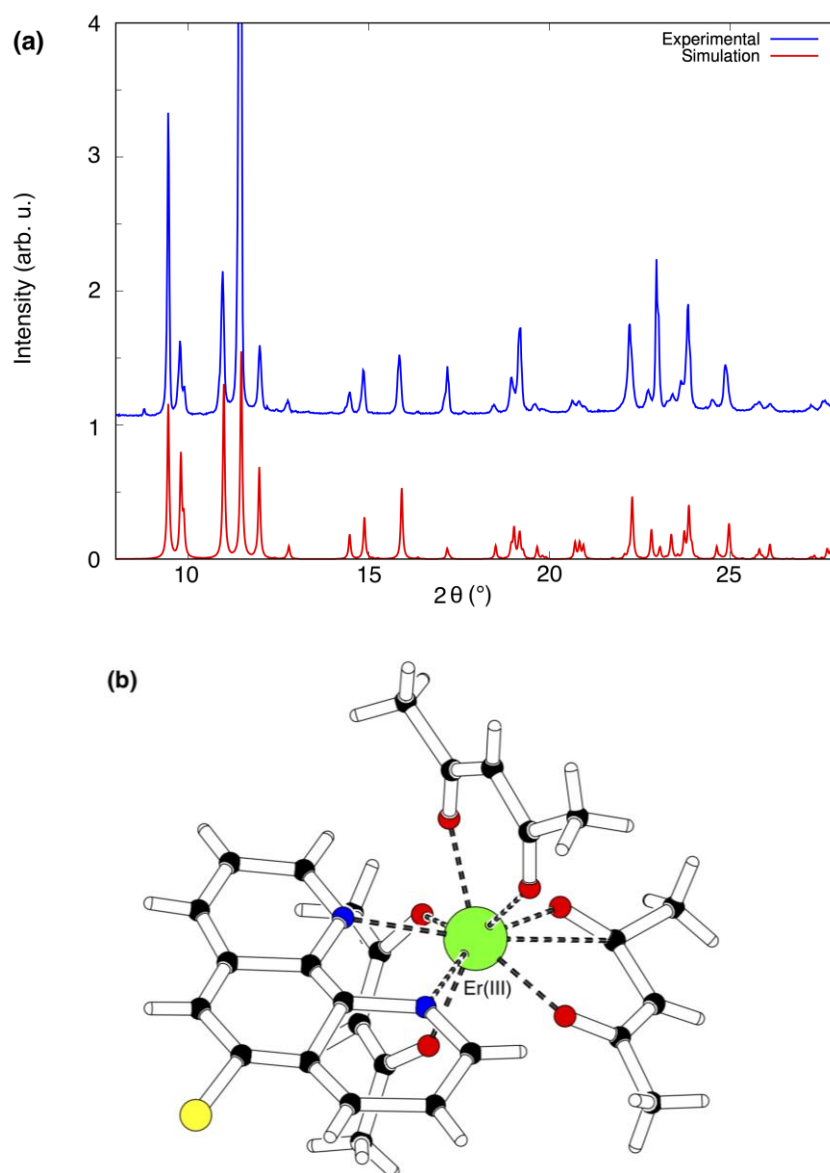
Raman spectra in the 25–3500  $\text{cm}^{-1}$  spectral range were acquired at room temperature using a LabRAM HR Evolution Raman microscope (Horiba, Fukuoka, Japan) and an 1800 gr/mm grating. The laser excitation at 532 nm was focused on the sample using a 50 $\times$  objective, and the laser power at the sample was less than 0.5 mW, resulting in no detectable heating or degradation of the sample. The average exposure time was 10 s, and 50 accumulations were used.

### 3. Computational Details

The geometry of the Er(III) complex was fully optimized at the DFT level of theory with the BP86 [22,23] exchange-correlation functional, using the 4*f*-in-core effective core potential (ECP) of Dolg et al. and the associated [5s4p3d]-GTO valence basis sets for the lanthanide [25] together with the 6–311++G(d,p) extended triple- $\zeta$  plus polarization basis sets for chlorine, oxygen, nitrogen, carbon, and hydrogen. This functional and ECP were chosen based on the reported benchmarking studies [26]. The inclusion of the *f* electrons in the core of the ECP is reasoned by the limited radial extension of the 4*f* orbitals (with radial maxima at around 50 pm) and their almost negligible participation in chemical bonding [27]. The Hessian matrix was calculated for the resultant stationary points to verify that they were minima, and the harmonic Raman spectra were also obtained and used to construct the computationally predicted spectra shown in the figures, which were simulated using Lorentzian functions with a full-width-at-half-maximum (FWHM) of 4  $\text{cm}^{-1}$  centered at the calculated wavenumbers. Chemcraft (Version 1.8) software was used to correct the intensities of the computed spectrum, taking into account the ambient temperature and laser wavelength [28]. All the calculations were carried out in vacuo using the Gaussian 16 code [29].

### 4. Results and Discussion

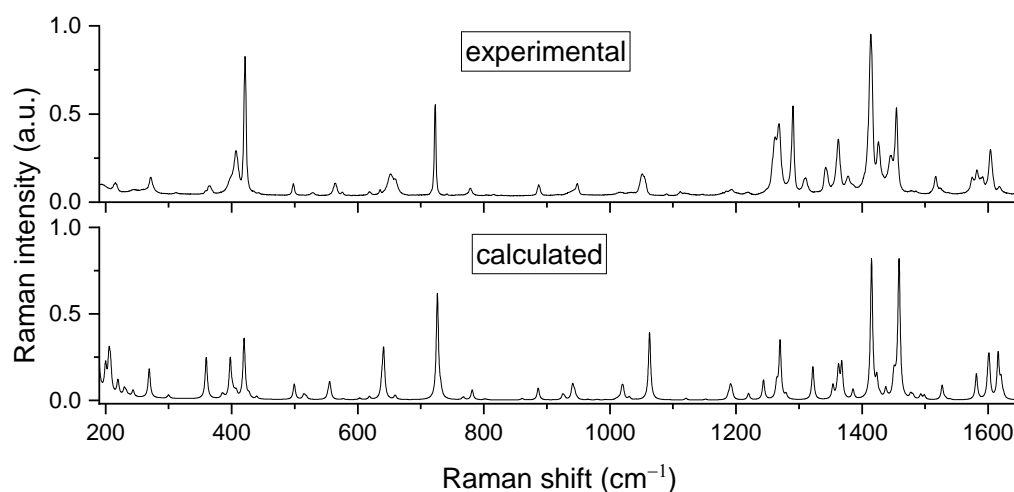
The crystallographic structure is monoclinic (noncentrosymmetric space group  $P2_1$ ), with cell parameters  $a = 9.6365(5)$ ,  $b = 30.855(2)$ ,  $c = 19.4378(9)$  Å, and  $\beta = 103.771(3)^\circ$ . The unit cell contains four independent crystallographic Er(acac)<sub>3</sub>(cphen) units, and no solvent molecules are incorporated in the crystal structure. Figure 1a shows the powder XRD pattern obtained for the erbium(III) complex and that simulated from the structure determined in the single-crystal XRD study. The calculated and measured XRD patterns match closely, apart from a few small peaks (the most prominent at 8.7°) that likely correspond to unreacted Er(acac). A schematic view of the erbium(III) complex is presented in Figure 1b. The rare-earth ion is eightfold coordinated by three acetylacetonate mononegative ions and one neutral 5-chloro-1,10-phenanthroline molecule with the chelation occurring via the N and O atoms.



**Figure 1.** (a) Experimental powder XRD patterns for the erbium(III) complex in comparison to the calculated pattern for the structure determined by single-crystal XRD (for clarity, the experimental data were offset by one unit along the vertical axis). (b)  $\text{Er}(\text{acac})_3(\text{cphen})$  complex, showing the eightfold coordination of the rare-earth ion via the N and O atoms of the ligands (atom colors: Er(III)—green, O—red, N—blue, C—black, Cl—yellow, H—white).

The calculated Raman spectrum forecasts reasonably well the one obtained experimentally (Figure 2). Nevertheless, some regions of the experimental spectrum are not accurately replicated. This discrepancy can largely be attributed to the limitations of the applied calculation approach. In particular, the performed calculations predict vibrations of an isolated molecule, thereby overlooking the influence of the intermolecular interactions on the intrinsic molecular vibrations in the periodic crystalline structure. Moreover, the low-energy regions of the Raman spectrum are particularly anticipated to be affected by phonon vibrations of the crystal lattice, which were not possible to factor into the present computation method. It is noteworthy that these calculations of such large molecular complexes, as examined in this study, span only a few days, nonetheless yielding very reasonable results. Conversely, more specialized computational approaches tailored for solid-state analyses, such as fully periodic calculations on the crystalline structures that mitigate the aforementioned limitations, could necessitate several months of computational

time [30]. The experimentally observed multiple Raman peaks at 1516–1604  $\text{cm}^{-1}$  were previously attributed to the stretching of the CC, CN, and C=O bonds of the rings of *N,N*- and *O,O*-donor molecules of a similar complex where Er(III) ions were coordinated by six O atoms and two N atoms [31–33]. These assignments are also supported by our calculations (Figure 2). Additionally, according to our computations, the strong features at 1410–1460  $\text{cm}^{-1}$  are due to the bending vibration of numerous C–H bonds. In the literature, the experimentally observed Raman feature at 400–407  $\text{cm}^{-1}$  was tentatively assigned to (Er–N) modes [32,33]. In contrast, according to our estimations for the studied Er(III) complex, these modes contribute to the small Raman bands observed at 271 and 365  $\text{cm}^{-1}$ . Features at 215 and 407  $\text{cm}^{-1}$ , on the other hand, can be attributed to more complex vibrations of the whole Er(III) complex involving Er–O bending and stretching vibrations, respectively, which is consistent with the estimates for other Er complexes [34]. Stretching vibrations of the 5-chloro-1,10-phenanthroline fragment, involving Er–N vibrations, are responsible for the intense Raman bands at 421 and 722  $\text{cm}^{-1}$ . Thus, the observed Raman vibrations involving the Er(III) atom confirm its coordination with O and N atoms of the ligands.



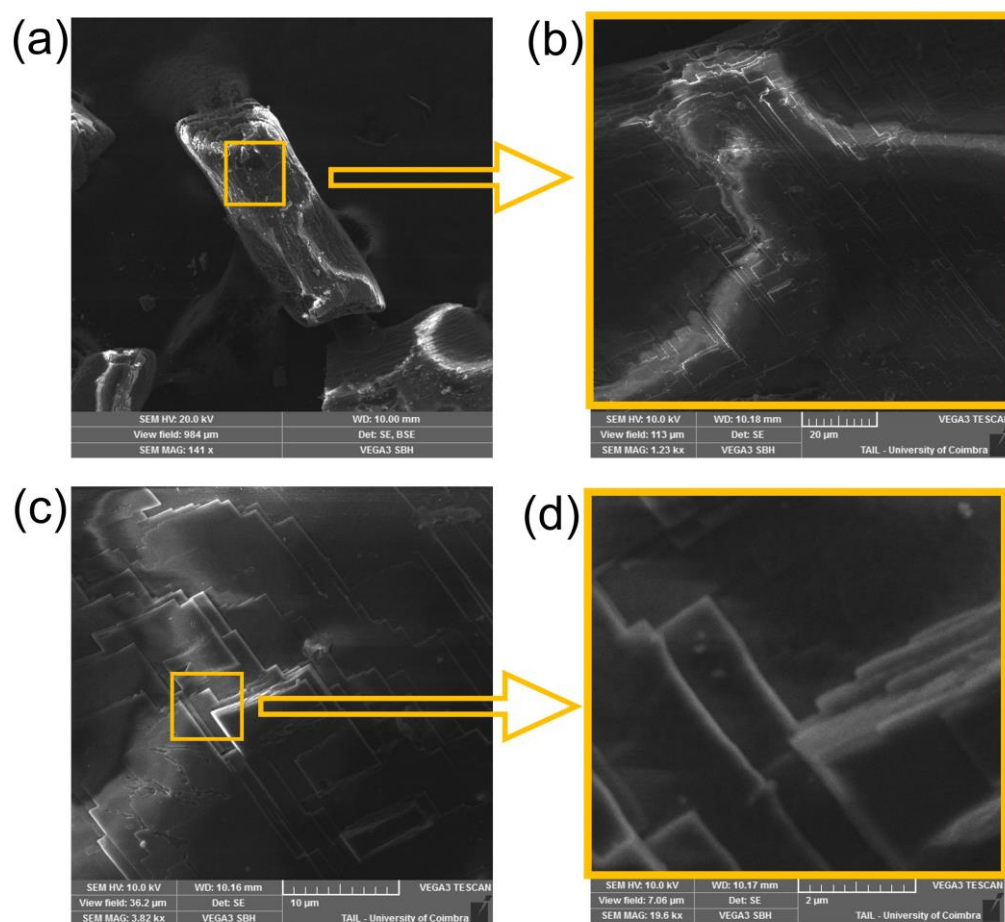
**Figure 2.** Experimental and calculated Raman spectra of Er(III) complex. The calculated spectrum was scaled by a factor of 1.02.

The results of the SEM imaging display the monoclinic shape of the erbium(III) complex crystal at the macroscale level (Figure 3a). The characteristic type of morphology at the higher magnification was observed (Figure 3b) to distinguish an organization of randomly distributed sheet layers (Figure 3c). Figure 3d shows the appearance of typical, for molecular structures, terrace–ledge morphology similar to those reported for other supramolecular and polar organic systems [21,35–38].

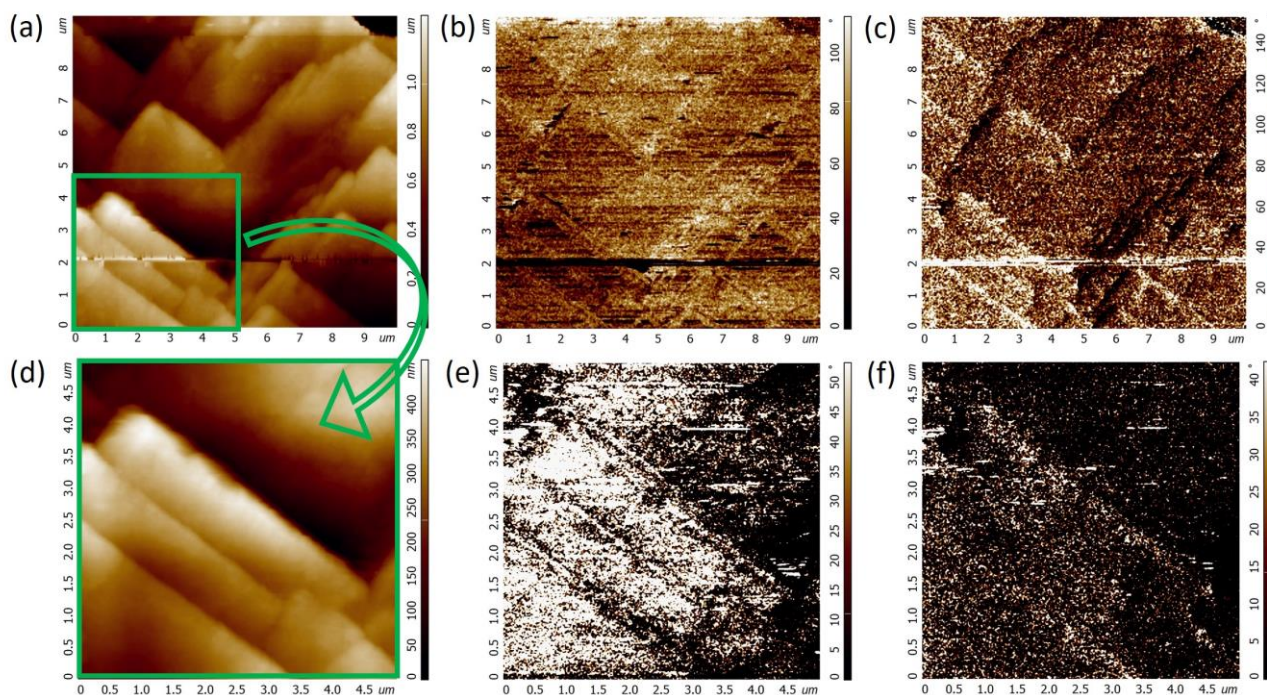
Consistent with the SEM results, the SPM scans disclose similar terrace–ledge morphology structures, represented in Figure 4. PFM scan images reveal correlated out-of-plane (OOP) (the corresponding phase component in Figure 4b,e) and in-plane (IP) (the corresponding phase component in Figure 4c,f) piezoresponses that were found to be in agreement with the noncentrosymmetric crystallographic structure of the erbium(III) complex. All the measured OOP and IP PFM components were affected by the terrace–ledge topography similar to those reported in some organic piezo- and ferroelectrics [35–38]. Figure 4d–f displays the distinct OOP PFM responses within two terrace–ledge structures, and the IP PFM responses reflect the boundary conditions.

To measure the local piezoelectric hysteresis, the switching spectroscopy PFM (SS-PFM) method was applied to the terrace–ledge structure according to the procedure described in ref. [39]. The results of the measurements at different points are presented in Figure 5. SS-PFM applied to the areas possessing opposite phases in OOP PFM response (a red circle and a blue square in Figure 5a) revealed robust and straight differences in magnitude (Figure 5c) and phase (Figure 5d). The corresponding direct piezoelectric coefficients ( $d_{33}^{eff}$ )

were measured at eight pm/V (at the area marked with the red circle) and five pm/V (at the area marked with the blue square). The local piezoelectric hysteresis measured at the compressed boundary condition between two terrace–ledge structures (a black circle in Figure 5a) revealed the absence of a hysteresis loop depending on the applied voltage (Figure 5b). This result points out the clamping effect on electric dipoles within compressed boundary conditions to give rise to the observation of strong piezoelectric behavior. To determine the influence of compressed boundary conditions on the SS-PFM results, the measurements at free and bulk boundary conditions were tested. For this, the SS-PFM measurements were conducted at two opposite edges of the terrace–ledge structures shown in Figure 5a at the places marked by a green triangle (free boundary conditions) and an inverted yellow triangle (bulk boundary conditions due to contact with a massive layer sheet). While a tiny hysteresis behavior was measured for both areas (see the phase signal in Figure 5f), the free grain boundary condition allows a higher amplitude of the PFM magnitude signal due to the absence of the tension forces. The corresponding direct piezoelectric coefficients ( $d_{33}^{eff}$ ) were measured at 4.5 pm/V for the free boundary condition and 4 pm/V for the bulk boundary condition.



**Figure 3.** Scanning electron microscopy images of the molecular erbium(III) complex  $\text{Er}(\text{acac})_3(\text{cphen})$  single crystal: (a) a single crystal view at  $\times 100$ , (b) a general image of the surface of the single crystal at  $\times 1000$ , (c) a terrace–ledge morphology structure of the surface visible at  $\times 5000$ , (d) a number of the steps of the terrace–ledge morphology structure distinguishable at  $\times 20,000$ .

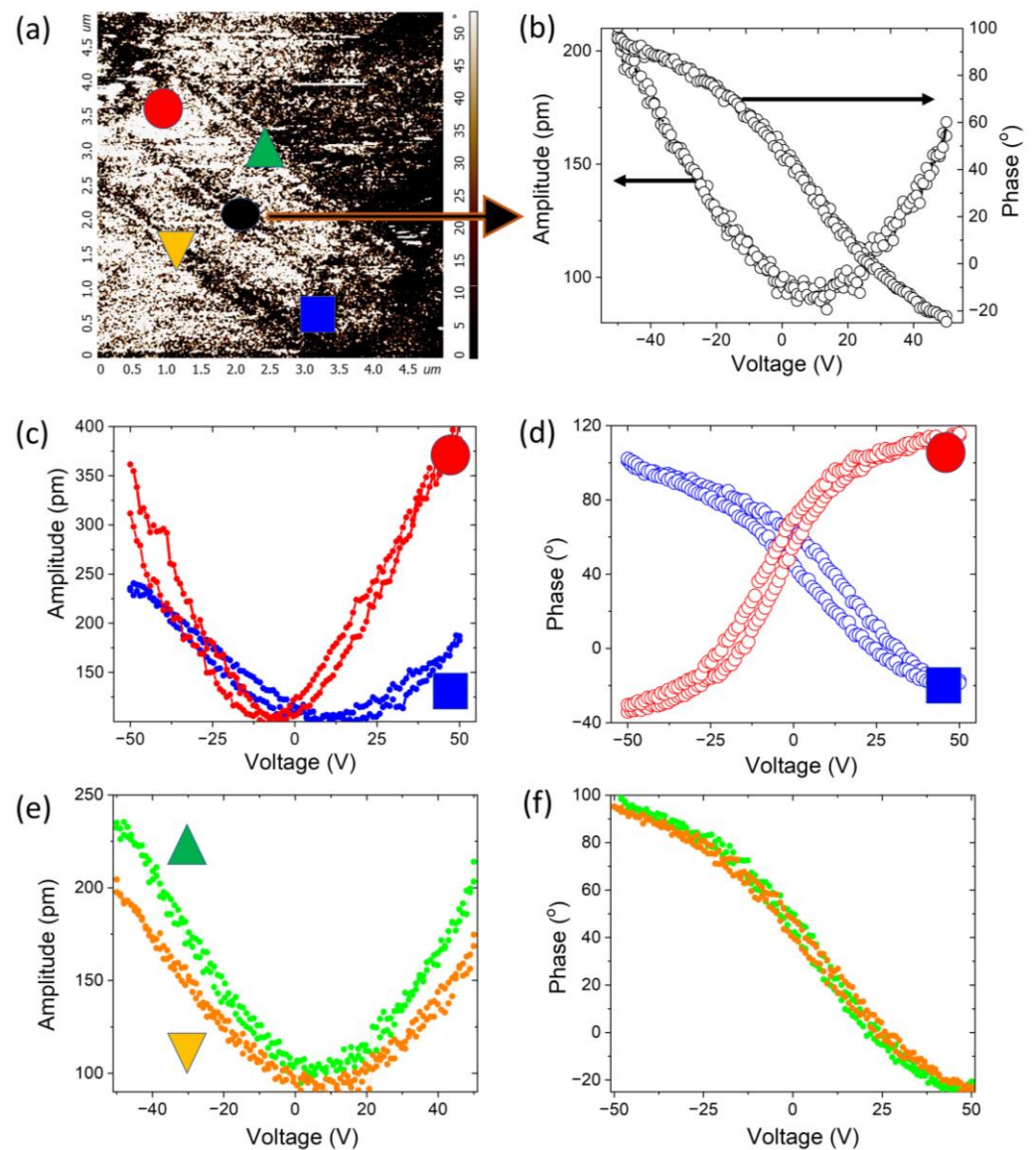


**Figure 4.** AFM and PFM scan images of terrace–ledge morphology structures in the erbium(III) complex: (a,d) topography and corresponding phase components for (b,e) out-of-plane and (c,f) in-plane PFM responses.

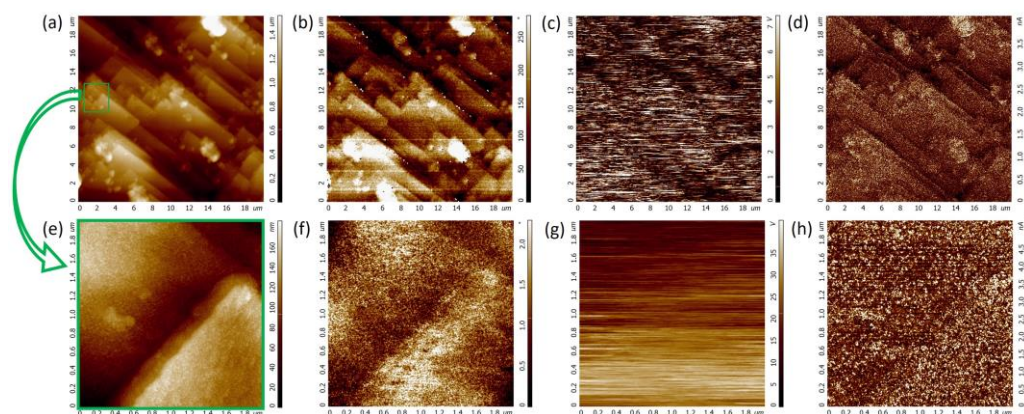
The electrophysical measurements have been conducted at micro- and nanoscale levels via EFM (surface charge distribution) and KPFM (surface potential distribution) approaches (Figure 6). The KPFM mode was utilized using the first (work function distribution) and second (dielectric permittivity and capacitance ( $dC/dz$ ) distributions) harmonics [40]. The results of the surface charge (Figure 6b) and  $dC/dz$  (Figure 6d) distributions measured at the microscale level show a distinct influence of the topography. This result reaffirms the strong influence of the terrace–ledge topography on the functional properties of the erbium(III) complex. Considering the surface potential distribution (Figure 6c), the regions with intense response can be associated with highly active polar regions, so-called hyperpolarized areas that are assumed to be very active in linear and nonlinear optical responses [41–43]. The magnified scan images disclose more details in the surface charge (Figure 6f) and  $dC/dz$  (Figure 6h) distributions. The enhanced EFM response is consistent with the increasing work function at the edge of the terrace–ledge structure, thus indicating the net of uncompensated surface charges (Figure 6f,g). The second harmonic KPFM signal mapping reveals a nanoscale clustering in the erbium(III) complex (Figure 6h).

Figure 7 shows the evolution of the scan scaling of Figure 6h to discover a phenomenon of nanoscale clustering in the erbium(III) complex. Figure 7e illustrates the sketch of what is seen in Figure 7c, where the localization of the Er ion is visualized via the  $dC/dz$  signal. SS-PFM measurements were acquired precisely in that place according to the probing scheme in Figure 7e, and the results of the magnitude and phase on the voltage dependencies are presented in Figure 7d. The characteristic ferroelectric behavior with strong hysteresis in both the magnitude and phase signals was measured, and the corresponding direct piezoelectric coefficient ( $d_{33}^{eff}$ ) was attained at 4 pm/V. Considering the maximum local piezoelectric coefficient measured at 8 pm/V, these results constitute the macroscopic polar properties of the erbium(III) complex to be 50% dependent on the Er ion and 50% on the ligand surrounding. The details of the exact spatial coordination between the lanthanide ion and its ligands ultimately define, in addition to the crystallographic symmetry determining the crystal packing in the solid state, the polar properties, hyperpolarizability, and linear and nonlinear optical properties of such lanthanide-based complexes.

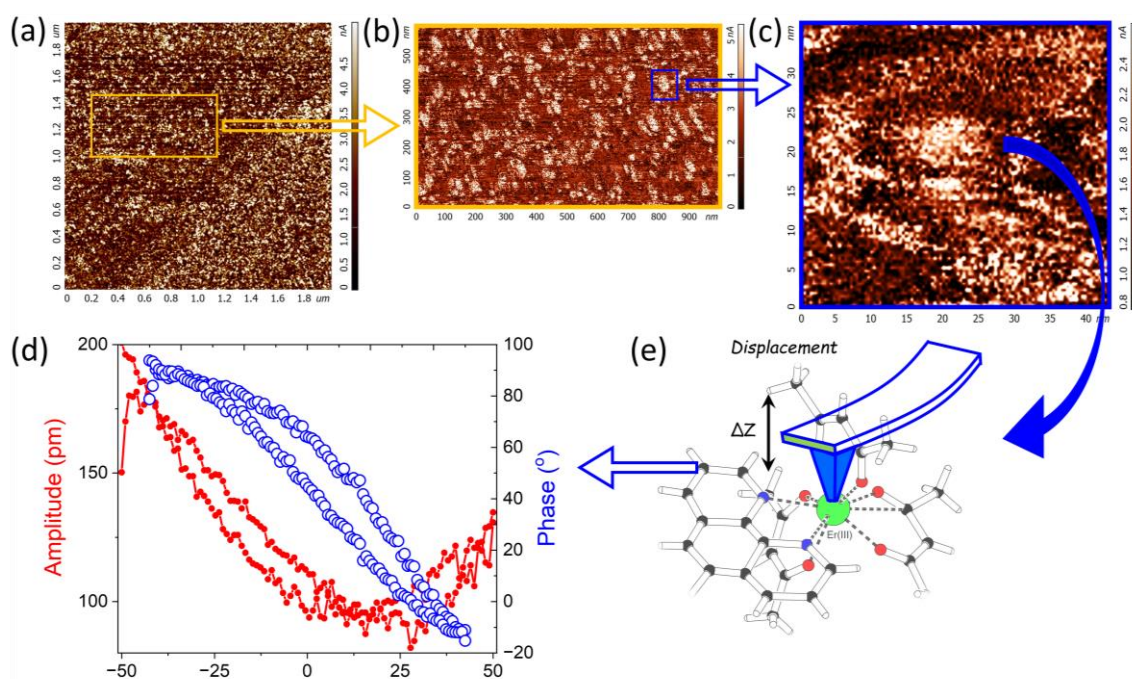




**Figure 5.** Switching spectroscopy PFM measurements: (a) schematic representation of the measured areas and the corresponding results of the (b,c,e) magnitude and (b,d,f) phase responses. Color legend: the red circle and the blue square correspond to the opposite phases in the OOP PFM response, the black circle points to the area of compressed boundary condition, the green triangle spots the free boundary condition, and the inverted yellow triangle marks the bulk boundary condition.



**Figure 6.** Electrophysical scan images of the erbium(III) complex: (a,e) topography and corresponding (b,f) surface charge, (c,g) surface potential, and (d,h) dC/dz distributions.



**Figure 7.** (a–c) Evolution of the dC/dz scan scaling to observe the clustering phenomenon in the erbium(III) complex. (d) Switching spectroscopy PFM data acquired on (e) localized Er ion in ligand surrounding (atom colors: Er(III)—green, O—red, N—blue, C—black, Cl—yellow, H—white).

## 5. Conclusions

To summarize, we successfully synthesized millimeter-sized single crystals of the molecular erbium(III) complex  $\text{Er}(\text{acac})_3(\text{cphen})$  and conducted complete investigations of polar and electronic properties at the macro-, micro-, and nanoscale levels. To achieve this, we applied very different but comprehensive methods such as X-ray diffraction, scanning electron microscopy, atomic force microscopy, as well as Raman spectroscopy. The atomic force microscopy method was implemented in several modes: semicontact force mode for the topography measurements, piezoelectric force mode for the measurements of the intrinsic and induced piezo- and ferroelectric properties, kelvin probe mode to study the surface potential distribution, and dC/dz mode for the capacitance distribution. We have demonstrated the monoclinic (noncentrosymmetric space group  $P2_1$ ) crystallographic structure and terrace–ledge morphology of the synthesized molecular erbium(III) complex crystals. By using the piezoelectric force microscopy (PFM) mode, the origins of the polar properties and hyperpolarizability in the synthesized samples were assigned to the internal domain structure framed by the characteristic terrace–ledge topography. The

direct piezoelectric coefficient ( $\sim d_{33}$ ) was found to be intensely dependent on the local area and measured in the range of 4–8 pm/V. A nanoscale study using kelvin probe force and capacitance force ( $dC/dz$ ) microscopy modes revealed the effect of clustering in the erbium(III) complex. The PFM method applied solely to the Er ion revealed the corresponding direct piezoelectric coefficient ( $\sim d_{33}$ ) of about 4 pm/V. Considering the maximum piezoelectric coefficient measured in the erbium(III) complex at 8 pm/V, a conclusion about the significant role of the spatial coordination between the lanthanide ion and the ligands was drawn. This coordination between the lanthanide ion and the nitrogen and oxygen atoms was also confirmed by Raman spectroscopy supported by density functional theory calculations utilizing the BP86 exchange-correlation functional. The obtained results were found to be of very great importance for the utilization of molecular erbium(III) complex crystals in low-magnitude magnetic or electric field devices. This application has the potential to reduce the required energy and accelerate the processing switching in nonvolatile memory devices. The obtained findings also pave the way for further studies of coupled magnetic, polar, and optical properties in lanthanide-based complexes. In particular, the magnetic properties at room and low temperature of this new Er(III) complex deserve a thorough investigation.

**Author Contributions:** Software, L.L.G.J.; Formal analysis, L.L.G.J. and R.F.; Investigation, M.I., A.G., A.B. and T.N.; Resources, A.G.; Writing—original draft, A.G.; Writing—review & editing, M.I., A.B., T.N., L.L.G.J., R.F., P.M.V. and J.A.P.; Supervision, M.I., P.M.V. and J.A.P.; Project administration, M.I. and J.A.P.; Funding acquisition, P.M.V. and J.A.P.; All authors have read and agreed to the published version of the manuscript.

**Funding:** This research was funded by the project CICECO-Aveiro Institute of Materials, UIDB/50011/2020, UIDP/50011/2020, and & LA/P/0006/2020, financed by national funds through the FCT/MEC (PIDDAC). Access to the TAIL-UC facility funded under QREN-Mais Centro project ICT\_2009\_02\_012\_1890 is gratefully acknowledged. The Coimbra Physics Centre is supported by FCT through the projects UIDB/04564/2020 and UIDP/04564/2020 co-funded by COMPETE- UE. The Coimbra Chemistry Centre—Institute of Molecular Sciences (CQC—IMS) is supported by FCT through projects UIDB/00313/2020 and UIDP/00313/2020 co-funded by COMPETE, and funds awarded by FCT to the Associated Laboratory Institute of Molecular Sciences. This work was partially supported by the government task project number FSFZ-2023-0005. The IMS project LA/P/0056/2020 is also acknowledged. The authors also thank the Laboratory for Advanced Computing at University of Coimbra (<https://www.uc.pt/lca>) for providing computing resources.

**Data Availability Statement:** Experimental data supporting reported results are available on request.

**Conflicts of Interest:** The authors declare no conflict of interest.

## References

1. Zhang, Y.; Liu, S.; Zhao, Z.S.; Wang, Z.; Zhang, R.; Liu, L.; Han, Z.B. Recent Progress in Lanthanide Metal-Organic Frameworks and Their Derivatives in Catalytic Applications. *Inorg. Chem. Front.* **2021**, *8*, 590–619. [CrossRef]
2. Eliseeva, S.V.; Bünzli, J.-C.G. Lanthanide Luminescence for Functional Materials and Bio-Sciences. *Chem. Soc. Rev.* **2010**, *39*, 189–227. [CrossRef]
3. SeethaLekshmi, S.; Ramya, A.R.; Reddy, M.L.P.; Varughese, S. Lanthanide Complex-Derived White-Light Emitting Solids: A Survey on Design Strategies. *J. Photochem. Photobiol. C Photochem. Rev.* **2017**, *33*, 109–131. [CrossRef]
4. Zhang, Q.Y.; Huang, X.Y. Recent Progress in Quantum Cutting Phosphors. *Prog. Mater. Sci.* **2010**, *55*, 353–427. [CrossRef]
5. Sun, R.G.; Wang, Y.Z.; Zheng, Q.B.; Zhang, H.J.; Epstein, A.J. 1.54 Mm Infrared Photoluminescence and Electroluminescence from an Erbium Organic Compound. *J. Appl. Phys.* **2000**, *87*, 7589–7591. [CrossRef]
6. He, H.; Dubey, M.; Sykes, A.G.; May, P.S. Hybridization of Near-Infrared Emitting Erbium(III) and Ytterbium(III) Monoporphyrinate Complexes with Silica Xerogel: Synthesis, Structure and Photophysics. *Dalt. Trans.* **2010**, *39*, 6466. [CrossRef] [PubMed]
7. He, H.; May, P.S.; Galipeau, D. Monoporphyrinate Ytterbium(III) Complexes with New Ancillary Ligands: Synthesis, Structural Analysis and Photophysical Investigation. *Dalt. Trans.* **2009**, *24*, 4766–4771. [CrossRef]
8. Li, J.; Kong, M.; Yin, L.; Zhang, J.; Yu, F.; Ouyang, Z.-W.; Wang, Z.; Zhang, Y.-Q.; Song, Y. Photochemically Tuned Magnetic Properties in an Erbium(III)-Based Easy-Plane Single-Molecule Magnet. *Inorg. Chem.* **2019**, *58*, 14440–14448. [CrossRef]
9. Weymann, L.; Bergen, L.; Kain, T.; Pimenov, A.; Shuvaev, A.; Constable, E.; Szaller, D.; Mill, B.V.; Kuzmenko, A.M.; Ivanov, V.Y.; et al. Unusual Magnetoelectric Effect in Paramagnetic Rare-Earth Lanthanide. *Npj Quantum Mater.* **2020**, *5*, 61. [CrossRef]

10. Long, J.; Rouquette, J.; Thibaud, J.M.; Ferreira, R.A.S.; Carlos, L.D.; Donnadieu, B.; Vieru, V.; Chibotaru, L.F.; Konczewicz, L.; Haines, J.; et al. A High-Temperature Molecular Ferroelectric Zn/Dy Complex Exhibiting Single-Ion-Magnet Behavior and Lanthanide Luminescence. *Angew. Chem.-Int. Ed.* **2015**, *54*, 2236–2240. [CrossRef]
11. Xiong, Y.A.; Sha, T.T.; Pan, Q.; Song, X.J.; Miao, S.R.; Jing, Z.Y.; Feng, Z.J.; You, Y.M.; Xiong, R.G. A Nickel(II) Nitrite Based Molecular Perovskite Ferroelectric. *Angew. Chem.-Int. Ed.* **2019**, *58*, 8857–8861. [CrossRef] [PubMed]
12. Bottaro, G.; Rizzo, F.; Cavazzini, M.; Armelao, L.; Quici, S. Efficient Luminescence from Fluorene- and Spirobifluorene-Based Lanthanide Complexes upon Near-Visible Irradiation. *Chem.-A Eur. J.* **2014**, *20*, 4598–4607. [CrossRef]
13. Wang, K.F.; Liu, J.-M.; Ren, Z.F. Multiferroicity: The Coupling between Magnetic and Polarization Orders. *Adv. Phys.* **2009**, *58*, 321–448. [CrossRef]
14. Abdullaev, D.A.; Milovanov, R.A.; Volkov, R.L.; Borgardt, N.I.; Lantsev, A.N.; Vorotilov, K.A.; Sigov, A.S. Ferroelectric Memory: State-of-the-Art Manufacturing and Research. *Russ. Technol. J.* **2020**, *8*, 44–67. [CrossRef]
15. Khomskii, D. Classifying Multiferroics: Mechanisms and Effects. *Physics* **2009**, *2*, 20. [CrossRef]
16. Fiebig, M.; Lottermoser, T.; Meier, D.; Trassin, M. The Evolution of Multiferroics. *Nat. Rev. Mater.* **2016**, *1*, 16046. [CrossRef]
17. Lu, C.; Hu, W.; Tian, Y.; Wu, T. Multiferroic Oxide Thin Films and Heterostructures. *Appl. Phys. Rev.* **2015**, *2*, 021304. [CrossRef]
18. Pyatakov, A.P.; Zvezdin, A.K. Magnetolectric and Multiferroic Media. *Uspekhi Fiz. Nauk* **2012**, *182*, 593. [CrossRef]
19. Rivera, J.-P. A Short Review of the Magnetolectric Effect and Related Experimental Techniques on Single Phase (Multi-) Ferroics. *Eur. Phys. J. B* **2009**, *71*, 299–313. [CrossRef]
20. Eerenstein, W.; Mathur, N.D.; Scott, J.F. Multiferroic and Magnetolectric Materials. *Nature* **2006**, *442*, 759–765. [CrossRef]
21. Long, J.; Ivanov, M.S.; Khomchenko, V.A.; Mamontova, E.; Thibaud, J.-M.; Rouquette, J.; Beaudhuin, M.; Granier, D.; Ferreira, R.A.S.; Carlos, L.D.; et al. Room Temperature Magnetolectric Coupling in a Molecular Ferroelectric Ytterbium(III) Complex. *Science* **2020**, *367*, 671–676. [CrossRef] [PubMed]
22. Becke, A.D. Density-Functional Exchange-Energy Approximation with Correct Asymptotic Behavior. *Phys. Rev. A* **1988**, *38*, 3098–3100. [CrossRef] [PubMed]
23. Perdew, J.P. Density-Functional Approximation for the Correlation Energy of the Inhomogeneous Electron Gas. *Phys. Rev. B* **1986**, *33*, 8822–8824. [CrossRef] [PubMed]
24. Soergel, E. Piezoresponse Force Microscopy (PFM). *J. Phys. D Appl. Phys.* **2011**, *44*, 464003. [CrossRef]
25. Dolg, M.; Stoll, H.; Savin, A.; Preuss, H. Energy-Adjusted Pseudopotentials for the Rare Earth Elements. *Theor. Chim. Acta* **1989**, *75*, 173–194. [CrossRef]
26. Kovács, A.; Klotzbücher, W. Octa-Coordination in Complexes of Lanthanides with N<sub>2</sub> Confirmed by Matrix-Isolation IR Spectroscopy and DFT Calculations. *J. Mol. Struct.* **2023**, *1272*, 134222. [CrossRef]
27. Kovács, A.; Konings, R.J.M. Structure and Vibrations of Lanthanide Trihalides: An Assessment of Experimental and Theoretical Data. *J. Phys. Chem. Ref. Data* **2004**, *33*, 377–404. [CrossRef]
28. Chemcraft-Graphical Software for Visualization of Quantum Chemistry Computations. Version 1.8, Build 654. Available online: <https://www.chemcraftprog.com> (accessed on 1 June 2023).
29. Frisch, M.J.; Trucks, G.W.; Schlegel, H.B.; Scuseria, G.E.; Robb, M.A.; Cheeseman, J.R.; Scalmani, G.; Barone, V.; Petersson, G.A.; Nakatsuji, H.; et al. *Gaussian 16, Revision B.01*; Gaussian, Inc.: Wallingford, CT, USA, 2016.
30. Nogueira, B.A.; Lopes, S.M.M.; Lopes, S.; Nikitin, T.; Rodrigues, A.C.B.; Eusebio, M.E.S.; Paixão, J.A.; Pinho e Melo, T.M.V.D.; Milani, A.; Castiglioni, C.; et al. 2,4,6-Trinitro-N-(m-Tolyl)Aniline: A New Polymorphic Material Exhibiting Different Colors. *Cryst. Growth Des.* **2021**, *21*, 7269–7284. [CrossRef]
31. Martín-Ramos, P.; Lavín, V.; Ramos Silva, M.; Martín, I.R.; Lahoz, F.; Chamorro-Posada, P.; Paixão, J.A.; Martín-Gil, J. Novel Erbium(III) Complexes with 2,6-Dimethyl-3,5-Heptanedione and Different N,N-Donor Ligands for Ormosil and PMMA Matrices Doping. *J. Mater. Chem. C* **2013**, *1*, 5701. [CrossRef]
32. Martín-Ramos, P.; Miranda, M.D.; Silva, M.R.; Eusebio, M.E.S.; Lavín, V.; Martín-Gil, J. A New Near-IR Luminescent Erbium(III) Complex with Potential Application in OLED Devices. *Polyhedron* **2013**, *65*, 187–192. [CrossRef]
33. Pereira da Silva, P.S.; Martín-Ramos, P.; Silva, M.R.; Lavín, V.; Chamorro-Posada, P.; Martín-Gil, J. X-Ray Analysis, Molecular Modeling and NIR-Luminescence of Erbium(III) 2,4-Octanedionate Complexes with N,N-Donors. *Polyhedron* **2014**, *81*, 485–492. [CrossRef]
34. Martín-Ramos, P.; Coutinho, J.T.; Ramos Silva, M.; Pereira, L.C.J.; Lahoz, F.; da Silva, P.S.P.; Lavín, V.; Martín-Gil, J. Slow Magnetic Relaxation and Photoluminescent Properties of a Highly Coordinated Erbium (iii) Complex with Dibenzoylmethane and 2,2'-Bipyridine. *New J. Chem.* **2015**, *39*, 1703–1713. [CrossRef]
35. Horiuchi, S.; Tokura, Y. Organic Ferroelectrics. *Nat. Mater.* **2008**, *7*, 357–366. [CrossRef]
36. Horiuchi, S.; Tokunaga, Y.; Giovannetti, G.; Picozzi, S.; Itoh, H.; Shimano, R.; Kumai, R.; Tokura, Y. Above-Room-Temperature Ferroelectricity in a Single-Component Molecular Crystal. *Nature* **2010**, *463*, 789–792. [CrossRef]
37. Chen, S.; Zeng, X.C. Design of Ferroelectric Organic Molecular Crystals with Ultrahigh Polarization. *J. Am. Chem. Soc.* **2014**, *136*, 6428–6436. [CrossRef]
38. Tang, Y.Y.; Li, P.F.; Liao, W.Q.; Shi, P.P.; You, Y.M.; Xiong, R.G. Multiaxial Molecular Ferroelectric Thin Films Bring Light to Practical Applications. *J. Am. Chem. Soc.* **2018**, *140*, 8051–8059. [CrossRef]

39. Ivanov, M.S.; Silibin, M.V.; Khomchenko, V.A.; Nikitin, T.; Kalinin, A.S.; Karpinsky, D.V.; Bdikin, I.; Polyakov, V.V.; Fausto, R.; Paixão, J.A. Strong Impact of LiNbO<sub>3</sub> Fillers on Local Electromechanical and Electrochemical Properties of P(VDF-TrFe) Polymer Disclosed via Scanning Probe Microscopy. *Appl. Surf. Sci.* **2019**, *470*, 1093–1100. [CrossRef]
40. Magonov, S.; NT-MDT Development. Magonov Single-Pass Measurements in Atomic Force Microscopy: Kelvin Probe Force Microscopy and Local Dielectric Studies. Available online: <https://www.ntmdt-si.com/resources/applications/single-pass-measurements-in-atomic-force-microscopy-kelvin-probe-force-microscopy-and-local-dielectric-studies> (accessed on 1 December 2022).
41. Wölfle, S.E.; Chaston, D.J.; Goto, K.; Sandow, S.L.; Edwards, F.R.; Hill, C.E. Non-Linear Relationship between Hyperpolarisation and Relaxation Enables Long Distance Propagation of Vasodilatation. *J. Physiol.* **2011**, *589*, 2607–2623. [CrossRef]
42. Xu, J.; Semin, S.; Niedzialek, D.; Kouwer, P.H.J.; Fron, E.; Coutino, E.; Savoini, M.; Li, Y.; Hofkens, J.; Uji-I, H.; et al. Self-Assembled Organic Microfibers for Nonlinear Optics. *Adv. Mater.* **2013**, *25*, 2084–2089. [CrossRef]
43. Xu, J.; Semin, S.; Cremers, J.; Wang, L.; Savoini, M.; Fron, E.; Coutino, E.; Chervy, T.; Wang, C.; Li, Y.; et al. Controlling Microsized Polymorphic Architectures with Distinct Linear and Nonlinear Optical Properties. *Adv. Opt. Mater.* **2015**, *3*, 948–956. [CrossRef]

**Disclaimer/Publisher’s Note:** The statements, opinions and data contained in all publications are solely those of the individual author(s) and contributor(s) and not of MDPI and/or the editor(s). MDPI and/or the editor(s) disclaim responsibility for any injury to people or property resulting from any ideas, methods, instructions or products referred to in the content.